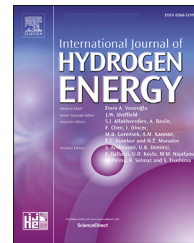


Available online at www.sciencedirect.com**ScienceDirect****ELSEVIER**journal homepage: www.elsevier.com/locate/he

Synthesis of the highly efficient catalysts CdZnS@MIL-53(Fe) and ZnS@MIL-53(Fe) and their thermally decomposed derivative for electrochemical OER activity and photodegradation of Rhodamine B dye

Ghulam Asghar ^a, Muhammad Fiaz ^b, Muhammad Asim Farid ^c,
Muhammad Naeem Ashiq ^a, Muhammad Athar ^{d,e,*}

^a Institute of Chemical Sciences, Bahauddin Zakariya University, Multan 60800, Pakistan

^b Department of Chemistry, Ajou University, Suwon 16499, South Korea

^c Department of Chemistry, Division of Science and Technology, University of Education Lahore, Pakistan

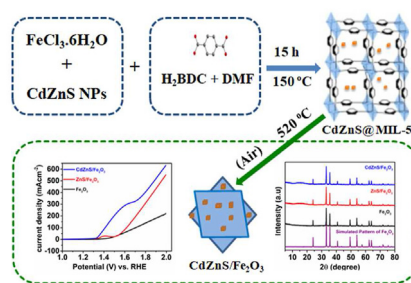
^d Laboratory for Catalysis and Sustainable Chemistry, Paul Scherrer Institut, 5232 Villigen-PSI, Switzerland

^e Institute for Chemical and Bioengineering, ETH Zurich, Vladimir Prelog Weg 1, 8093 Zurich, Switzerland

HIGHLIGHTS

- Designing of highly efficient catalysts by in-situ incorporation of CdZnS nanoparticles in (MIL-53(Fe)).
- The newly designed CdZnS@MIL-53(Fe) and its derivative CdZnS/Fe₂O₃ showed efficient OER activity.
- The CdZnS/Fe₂O₃ is also effective for photodegradation of Rhodamine B (up to 75% in just 80 min).
- The better catalytic activity is due to formation of heterojunction between CdZnS and MIL-53(Fe) or its derivative.

GRAPHICAL ABSTRACT



ARTICLE INFO

Article history:

Received 23 July 2023

Received in revised form

3 September 2023

ABSTRACT

The development of a highly efficient catalyst for water splitting and photodegradation of organic dyes has become the focus of a considerable number of research groups. In the work described here CdZnS@MIL-53(Fe) and ZnS@MIL-53(Fe) were synthesized by the solvothermal method and subjected to thermal degradation at 520 °C in an oxidative environment to obtain CdZnS/Fe₂O₃ and ZnS/Fe₂O₃, respectively. Electrocatalytic activity for

* Corresponding author. Laboratory for Catalysis and Sustainable Chemistry, Paul Scherrer Institut, 5232 Villigen-PSI, Switzerland.

E-mail address: athar.qr@gmail.com (M. Athar).

<https://doi.org/10.1016/j.ijhydene.2023.09.208>

0360-3199/© 2023 The Authors. Published by Elsevier Ltd on behalf of Hydrogen Energy Publications LLC. This is an open access article under the CC BY license (<http://creativecommons.org/licenses/by/4.0/>).

Accepted 19 September 2023
Available online 4 October 2023

Keywords:
MIL-53(Fe)
MOF derivative
Rhodamine B
Photodegradation
Electrochemical oxygen evolution reaction

the oxygen evolution reaction is analyzed via cyclic voltammetry and linear sweep voltammetry. It was found that CdZnS@MIL-53(Fe) shows maximum catalytic activity for the oxygen evolution reaction and delivers 10 mAcm^{-2} current density at 95 mV overpotential as compared to MIL-53(Fe)/NF (210 mV) and ZnS@MIL-53(Fe)/NF (112 mV). Similarly, the derivative of it, CdZnS/Fe₂O₃, shows maximum catalytic activity for the oxygen evolution reaction and delivers 10 mAcm^{-2} current density at 90 mV overpotential as compared to Fe₂O₃ (204 mV) and ZnS/Fe₂O₃ (115 mV). Based on these results, it is evident that these materials are highly efficient for OER activity compared with other materials in literature. Similarly, CdZnS/Fe₂O₃ shows maximum photocatalytic activity for the photodegradation of Rhodamine B, up to 75% compared to CdZnS@MIL-53(Fe), which degrades up to 51% of the dye. The synthesized materials were characterized by powdered X-ray diffraction, Fourier transform infrared spectroscopy and scanning electron microscopy. Based on these results the aim is to develop more MOF-based materials and their derivatives by simple heat treatment and to implement them in different catalytic applications.

© 2023 The Authors. Published by Elsevier Ltd on behalf of Hydrogen Energy Publications LLC. This is an open access article under the CC BY license (<http://creativecommons.org/licenses/by/4.0/>).

1. Introduction

The energy crisis and environmental pollution are two major problems, which researchers are trying to alleviate [1]. Energy demands are continuing to increase due to rapid population growth. At present, resources are insufficient to meet these demands. The burning of fossil fuels emits carbon monoxide (CO) and carbon dioxide (CO₂) with their deleterious effects on the environment [2,3]. Therefore, the generation of alternate environmentally friendly renewable energy is a challenge that must be met [4–7]. Among the different strategies, the generation of hydrogen and oxygen by water splitting is the focus of much current research [8–11]. Water splitting consists of two half reactions: the hydrogen evolution reaction (HER) and the oxygen evolution reaction (OER), both of which require overpotential to take place at a suitable rate. This is particularly true for OER, a 4-electron coupled reaction, which requires a much higher over-potential compared to HER. Thus, the development of an efficient OER catalyst, requiring a very low over-potential, is an important challenge. Another major crisis is water pollution by industrial effluents such as dyes. Of the organic dyes, Rhodamine B is very toxic and causes serious health conditions, such as kidney failure, hormonal imbalance and dermatologic problems. Ways must be found to degrade harmful dyes by environmentally friendly methods [12]. Solar-light active catalysts have proved to be one of the best ways of removing dyes from water. Catalytic materials, such as TiO₂, ZnO, NiO₂, CdS and graphene oxide, have been studied for the production of hydrogen and oxygen by water splitting. However, their catalytic activity is still too low due to limitations such as a high band gap, a high rate of electron-hole pair recombination and expense [13–15]. Different strategies are being used to improve the efficiency of catalysts, including doping, heterojunction formation, composite formation and sensitization with dye [16–19]. Doping of gold nanoparticles in ZnO nanowires showed eight times more activity compared to ZnO nanoparticles [20]. Heterojunction formation is another important strategy to increase the catalytic efficiency of, for

example, CdS/ZnS, which has a higher catalytic activity than an individual particle [21,22]. Metal organic frameworks (MOFs) consist of a metal cluster combined with an organic linker. These materials are suitable for use in a number of applications, including gas adsorption, drug delivery and photocatalytic activity; this is due to their uniformity, porosity and high surface area [23]. MOF-based materials are reported to be efficient OER catalysts. One example is the NiS@MOF-5 catalyst, which required a very low overpotential of 174 mV to deliver 10 mAcm^{-2} current density [24]. MOF-based materials are also promising for the degradation of organic dyes. MIL53, an iron-containing MO, showed better photocatalytic activity and removed 80% of Rhodamine B in four cycles. MIL-53(Fe) is solar-light energetic due to its central metal-oxo cluster, which enables charge transfer. MIL-68(Fe) is also a good photoelectrocatalyst for a number of applications because of its lower absorption edge as a result of transition between d-d orbitals [25]. In addition to these MOF-based composites, highly active derivatives of MOF are obtained by heat treatment of bare MOFs as well as a nonmaterial@MOF composite such as the ZIF-derived ZnS–CdS were fabricated and showed better current density at the lowest overpotential [26–28]. Fe₂O₃/TiO₂ and Fe₂O₃/C composites are obtained by heat treatment of MIL-101(Fe) at 600 and 500 °C and showed remarkable photocatalytic activity [29].

Here we report the synthesis of efficient catalytic materials by thermal degradation: CdZnS@MIL-53(Fe) and ZnS@MIL-53(Fe) and their respective derivatives CdZnS/Fe₂O₃ and ZnS/Fe₂O₃. These materials were applied to study OER activity for electrochemical water splitting and the photodegradation of Rhodamine B.

2. Experimental methods

2.1. Chemicals

All the chemicals used for the synthesis of ZnS nanoparticles, CdZnS nanoparticles, MIL-53(Fe), ZnS@MIL-53(Fe) and

CdZnS@MIL-53(Fe) were purchased from Merck: iron chloride hexahydrate ($\text{FeCl}_3 \cdot 6\text{H}_2\text{O}$; 98%), benzene-1,4-dicarboxylic acid (H_2BDC ; 97%), zinc acetate dihydrate ($\text{Zn}(\text{CH}_3\text{COO})_2 \cdot 2\text{H}_2\text{O}$; 97%), cadmium acetate dihydrate ($\text{Cd}(\text{CH}_3\text{COO})_2 \cdot 2\text{H}_2\text{O}$; 99%), sodium sulphide pentahydrate, ($\text{Na}_2\text{S} \cdot 5\text{H}_2\text{O}$; 96%), terephthalic acid ($\text{C}_8\text{H}_6\text{O}_4$; 99%), thiourea ($\text{CH}_4\text{N}_2\text{S}$; 98%), N,N-dimethylformamide ($\text{C}_3\text{H}_7\text{NO}$; 97%), ethanol ($\text{CH}_3\text{CH}_2\text{OH}$; 96%) and deionized water.

2.2. Preparation of ZnS nanoparticles

ZnS nanoparticles were synthesized by the hydrothermal method [30,31]. Zinc acetate hydrate (1.10 g, 5 mmol) was dissolved in 15 mL of deionized water under continuous stirring. Another solution, made by dissolving sodium sulphide pentahydrate (0.84 g, 5 mmol) in 15 mL deionized water, was added to the above solution while stirring. The white suspension was transferred to a Teflon-lined autoclave and heated at 170 °C for 3 h. White powder formed, which was separated by centrifugation, washed with deionized water and dried.

2.3. Preparation of CdZnS nanoparticles

CdZnS nanoparticles were synthesized by co-precipitation [32]. Zinc acetate dihydrate (1.10 g, 5 mmol) and cadmium acetate dihydrate (0.95 g, 5 mmol) were dissolved in 30 mL of deionized water under continuous stirring. Another solution, made by dissolving sodium sulphide pentahydrate (0.84 g, 5 mmol) in 15 mL deionized water, was added to the above solution while stirring constantly. The two solutions were then mixed and stirred for 20 min to obtain a homogenous mixture. Then 2 mL of mercaptoethanol (capping agent) were added drop-wise to the above mixture, which was stirred for 2 h at room temperature. Orange crystals formed and were separated by centrifugation, washed with deionized water and dried overnight at 70 °C.

2.4. Preparation of MIL-53(Fe), ZnS@MIL-53(Fe) and CdZnS@MIL-53(Fe)

A solvothermal process was used to synthesize MIL-53(Fe), ZnS@MIL-53(Fe) and CdZnS@MIL-53(Fe). For MIL-53(Fe), iron chloride hexahydrate (1.21 g, 4.47 mmol) was dissolved in 35 mL DMF. In another flask, benzene-1,4-dicarboxylic acid (H_2BDC) (0.8 g, 4.82 mmol) was dissolved in 35 mL of DMF, and this solution was added drop-wise to the former solution while stirring. The mixture was transferred to a 100-mL Teflon-lined autoclave and heated at 150 °C for 15 h. The product was separated by centrifugation and washed twice with DMF and twice with methanol and then dried in vacuum oven at 80 °C.

ZnS@MIL-53(Fe) and CdZnS@MIL-53(Fe) were synthesized by the in-situ introduction of pre-synthesized ZnS and CdZnS into a host MOF. For this purpose, iron chloride hexahydrate (1.21 g, 4.47 mmol) was dissolved in 25 mL DMF while stirring. Meanwhile, a suspension of pre-synthesized nanoparticles (ZnS or CdZnS) was prepared by sonicating 0.01 g nanoparticles in 10 mL DMF, which was then poured into the above solution. Benzene-1,4-dicarboxylic acid (H_2BDC) (0.8 g, 4.82 mmol) was dissolved in 35 mL DMF and added dropwise to the above mixture while stirring. The mixture was transferred to a 100-mL Teflon-lined autoclave and heated at 150 °C for 15 h. Finally, the yellow/brown powders of both composites were separated by centrifugation, washed twice with DMF and twice with methanol and dried at 80 °C under vacuum for 12 h.

2.5. Heat treatment of MIL-53(Fe), ZnS@MIL-53(Fe) and CdZnS@MIL-53(Fe)

MIL-53(Fe), ZnS@MIL-53(Fe) and CdZnS@MIL-53(Fe) decomposed by heating in air in a furnace at 520 °C. Typically, 0.5 g of synthesized material was placed in an alumina crucible and heated from room temperature to 520 °C at a rate of 6 °C per minute. The material was kept at 520 °C for 2 h and cooled to room temperature at 10 °C per minute (see Fig. 1).

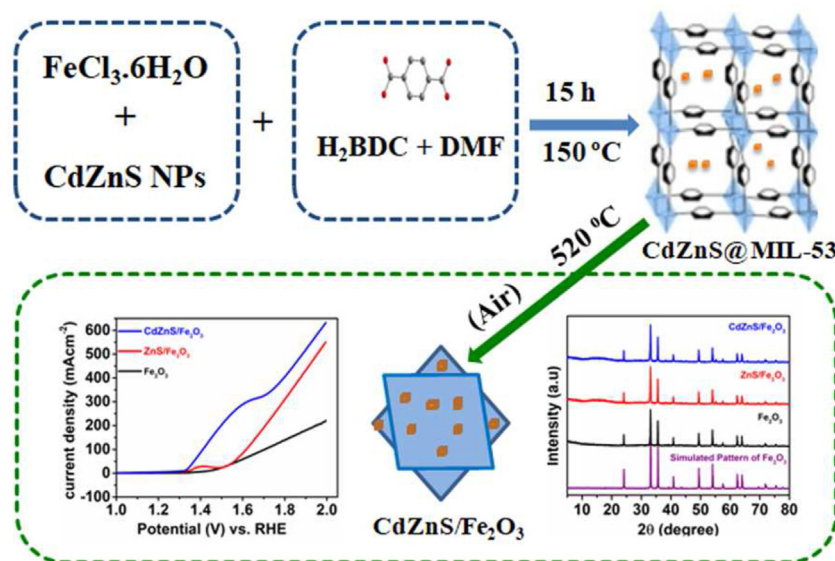


Fig. 1 – Schematic representation of synthesis of CdZnS/Fe₂O₃.

2.6. Fabrication of a working electrode

Electrochemical activity of the synthesized samples was studied by preparing working electrodes of the samples on nickel foam. A small piece ($1\text{ cm} \times 1\text{ cm}$) of nickel foam was washed with deionized water and acetone and dried at 100°C for 6 h. The sample (0.02 g) was mixed with a small amount of water and ground using a pestle and mortar to obtain a paste, which was spread uniformly on the Ni foam. This piece of nickel foam was used as a working electrode for OER analysis.

2.7. Electrochemical OER analysis

The electrochemical oxygen evolution test was carried out by using NOVA potentiostate with a three-electrode setup. Catalyst@Ni-foam was used as the working electrode, Pt wire as the counter electrode and Ag/AgCl as the reference electrode in 1.0 M KOH solution as the electrolyte. Cyclic voltammetry (CV) and linear sweep voltammetry were studied to analyze the electrochemical OER. CV was performed at a scan rate of 50 mVs^{-1} . All the data were converted to the reversible hydrogen electrode (RHE) according to the following equation [33]:

$$E_{\text{RHE}} = E_{\text{Ag/AgCl}} / \text{Sat. KCl} + 0.059 \text{ pH} + 0.197 \quad (1)$$

The overpotential (η) of OER was calculated by equation (2):

$$\eta = E_{\text{RHE}} - 1.23 \quad (2)$$

A Tafel plot was used to calculate the Tafel slope according to equation (3):

$$\eta = a + b \log j \quad (3)$$

where η is overpotential, j current density and b the Tafel slope.

2.8. Degradation of photocatalytic dye

In a typical procedure, 47.9 mg of Rhodamine B were dissolved in deionized water to make 1.0 L dye solution. Rhodamine B solution (100 mL) was poured into a flask and 0.02 g of the photocatalyst was added. The mixture was poured into a photoreactor while stirring continuously for 30 min in the dark. Three milliliters of suspension were taken and the solid particles were removed by filtering; absorbance was measured with a spectrophotometer at 554 nm. The dye solution was then illuminated with a 500 W tungsten lamp while stirring. The suspension (3 mL) was removed from the reactor at 10-min intervals and absorbance was measured. This procedure was repeated for 80 min.

2.9. Characterization

The synthesized materials were characterized by PXRD, FTIR, and SEM. PXRD was taken by means of a Bruker D8 advance diffractometer, in a 2θ range of 4° – 70° at a Cu $K\alpha$ radiation of $\lambda = 1.5406\text{ \AA}$, and a LYNXEYE XE detector. The operating voltage and the current of the X-ray tube were 40 kV and 40 mA,

respectively. Functional group identification was done by FTIR spectrometry (Nicolet Nexus 870) at a wavenumber of 400 – 4000 cm^{-1} . The Brunauer–Emmett–Teller (BET) surface area of the samples was determined by measuring the nitrogen sorption isotherms at 77 K on a Micromeritics Tristar II analyzer. Before starting the measurements, the samples were activated under vacuum at 120°C for 24 h [23]. The pore size distribution was calculated by the Barrett–Joyner–Halenda (BJH) method through the adsorption branch [34]. A scanning electron microscope (SEM), JSM-7100F JEOL, with carbon-coated samples, was used to study the morphology and size of the synthesized materials.

3. Results and discussion

3.1. Powder X-ray diffraction

Fig. 2 shows Powder X-ray Diffraction (PXRD) patterns of the synthesized samples as well as of their thermally treated derivatives. **Fig. 2(a)** reveals that the diffraction peaks for MIL-53 (Fe) are well matched with the simulated pattern of MIL-53 (Fe). Major diffraction peaks at 20° ; 9.24° , 12.40° , 17.01° , 25.50° and 27.31° with hkl values of (200), (120), (212), (240) and (141), respectively, are in good agreement with the reported pattern [CCDC No. 690316] [35]. However, there was small variation in some of the peaks as well as in the PXRD patterns due to the flexible nature of MIL-53(Fe) [36]. The diffraction pattern for MIL-53(Fe) is more pronounced than that of the incorporated nanoparticles in ZnS@MIL-153(Fe) and CdZnS@MIL-53 (Fe). **Fig. 2(b)** shows that bare MOF MIL-53(Fe) decomposes to Fe_2O_3 nanoparticles, as expected, because MIL-53 (Fe) contains a $[\text{Fe}(\text{OH})(\text{COOH})_6]$ central metallic cluster linked to the BDC ligand. The organic part decomposes to carbon dioxide and water, leaving behind Fe_2O_3 as the final product. All the diffraction peaks at 20° , i.e., 24.11° , 33.14° , 35.6° , 40.8° , 49.6° , 54.1° and 62.4° with hkl values of (012), (104), (110), (113), (024), (116) and (214), respectively, are in good agreement with the reported pattern [ICSD No. 201096] as well as with the simulated pattern of the Fe_2O_3 nanoparticles [37]. In the case of the thermally degraded ZnS@MIL-53 (Fe) and CdZnS@MIL-53 (Fe) it was assumed that composites of ZnS/ Fe_2O_3 and CdZnS/ Fe_2O_3 would be obtained [38].

However, the PXRD patterns of the derivatives of ZnS@MIL-53(Fe) and CdZnS@MIL-53 (Fe) reveal that all the diffraction peaks are indexed to Fe_2O_3 and peaks; there are no visible peaks for the ZnS and CdZnS nanoparticles. This is because there are only a very small number of ZnS and CdZnS nanoparticles and they are masked by Fe_2O_3 .

3.2. Fourier transfer infrared spectroscopy (FTIR)

Fig. 3(a–b) presents the FTIR spectra of the synthesized materials. In the FTIR spectrum of bare MOF MIL-53(Fe) (**Fig. 3(a)**) there are two dominant peaks at 1592 and 1383 cm^{-1} due to asymmetric (C=O) and symmetric (C—O) vibrations, respectively. Another vibrational peak is observed at 1678 cm^{-1} as a result of the stretching vibrations of the C=O of carboxylate ligand. A sharp peak at 745 cm^{-1} is due to the C—H bending vibrations of the benzene ring [39]. The peak at 542 cm^{-1}

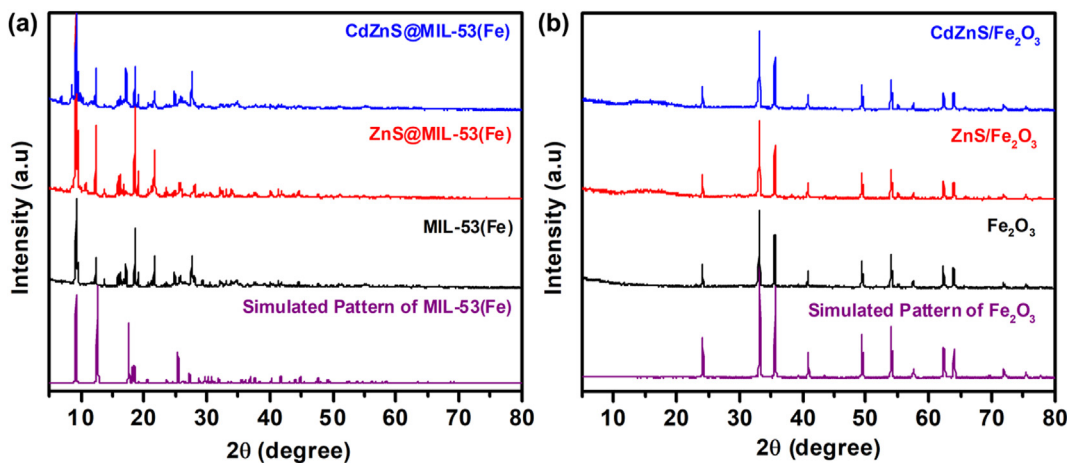


Fig. 2 – PXRD patterns of (a) original MOFs (MIL-53(Fe), ZnS@MIL-53(Fe) and CdZnS@MIL-53(Fe)) and (b) MOF derivatives (Fe₂O₃, ZnS/Fe₂O₃ and CdZnS/Fe₂O₃).

corresponds to the Fe-oxo cluster of MIL-53(Fe) [40]. Fig. 3(b) represents the FTIR spectra of MIL-53(Fe), ZnS@MIL-53(Fe) and CdZnS@MIL-53(Fe) after heat treatment and the conversion to Fe₂O₃, ZnS/Fe₂O₃ and CdZnS/Fe₂O₃, respectively. These spectra contain a strong vibrational peak at 543 cm⁻¹ and a weak vibrational peak at 695 cm⁻¹ due to the stretching vibrations of Fe–O indexed to the Fe₂O₃ nanoparticles [41,42].

3.3. Scanning electron microscopy

The morphology of all the synthesized materials was studied by scanning electron microscopy. Fig. 4(a-f) gives the SEM images of all the synthesized materials before and after heating. Fig. 4(a) presents the SEM image of bare MIL-53(Fe); it shows that it grew as well-defined and uniformly distributed tetrahedral crystals. However, after incorporation of ZnS and CdZnS, there are variations in the shape and size of the crystals (Fig. 4(b–c)), while, after heat treatment, all the

materials have an irregular block shape with a slight agglomeration (Fig. 4(d–f)).

3.4. Surface area and pore size distribution

The porosity of MIL-53(Fe), ZnS@MIL-53(Fe) and CdZnS@MIL-53(Fe) was studied by means of liquid nitrogen adsorption under standard conditions. An adsorption/desorption (BET) isotherm was measured for MIL-53(Fe), ZnS@MIL-53(Fe) and CdZnS@MIL-53(Fe), thus depicting the mesoporosity of the sample (Fig. 5). The BET surface area of 14.6 m²/g, 10.2 m²/g and 5.9 m²/g was found for MIL-53(Fe), ZnS@MIL-53(Fe) and CdZnS@MIL-53(Fe), respectively. The adsorption/desorption isotherms exhibit a slight hysteresis loop with condensation under a relative P/P₀ pressure of 0.0–1.0; the shape of the curves suggests the mesoporous structure of the synthesized materials. This phenomenon is often referred to as the Tensile Strength Effect (TSE) [43,44]. A cumulative pore volume of

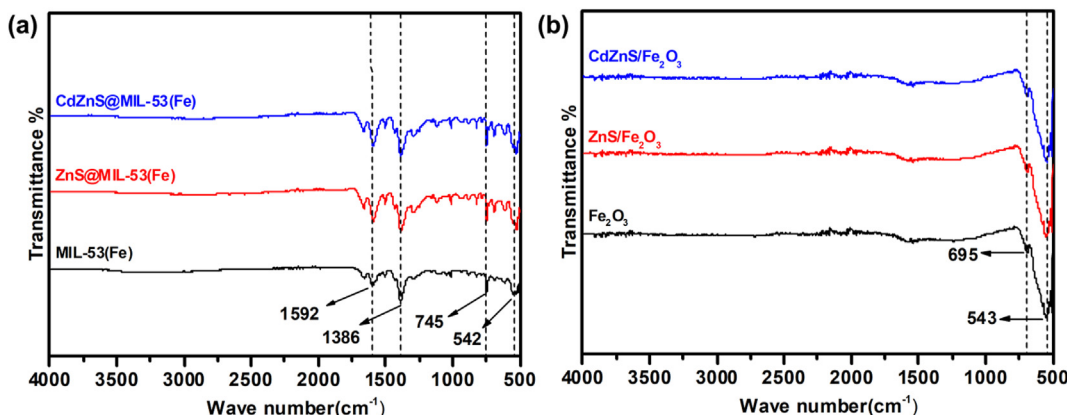


Fig. 3 – FTIR spectra of (a) original MOFs, MIL-53(Fe), ZnS@MIL-53(Fe) and CdZnS@MIL-53(Fe), and (b) MOF derivatives Fe₂O₃, ZnS/Fe₂O₃ and CdZnS/Fe₂O₃.

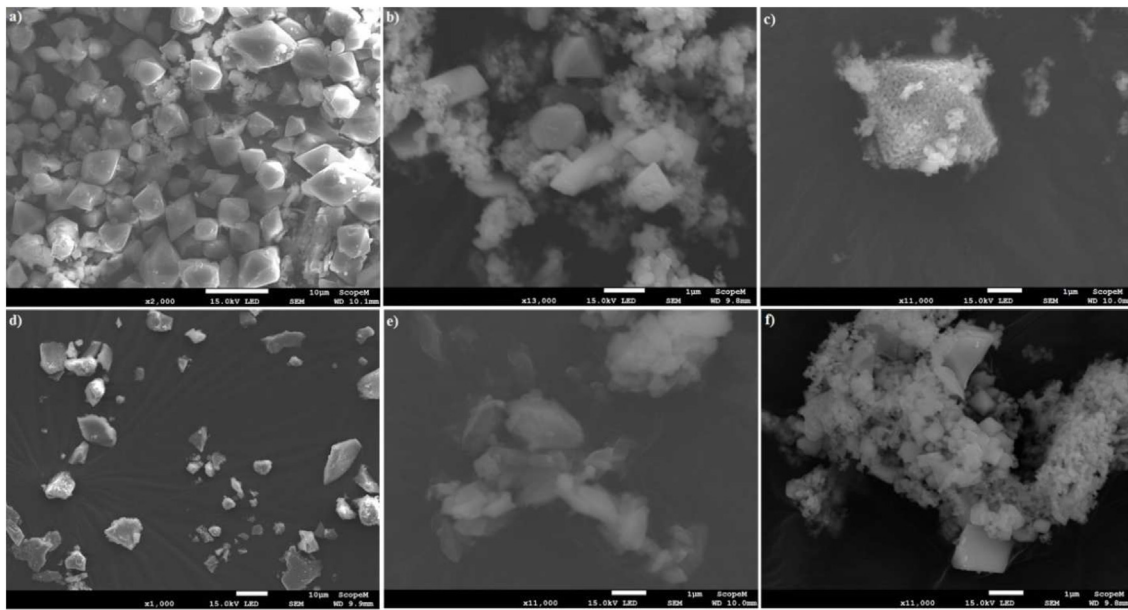


Fig. 4 – SEM images of (a–c) original MOFs MIL-53(Fe), ZnS@MIL-53(Fe) and CdZnS@MIL-53(Fe) and (d–f) MOF derivatives Fe_2O_3 , $\text{ZnS}/\text{Fe}_2\text{O}_3$ and $\text{CdZnS}/\text{Fe}_2\text{O}_3$.

19.3, 18.8 and 7.4 cm^3/mg was found for MIL-53(Fe), ZnS@MIL-53(Fe) and CdZnS@MIL-53(Fe), respectively. The results are in good agreement with the findings derived from the

adsorption/desorption isotherm in Fig. 5, which is indicative of a mesoporous structure. Table 1 lists the BET and BJH parameters.

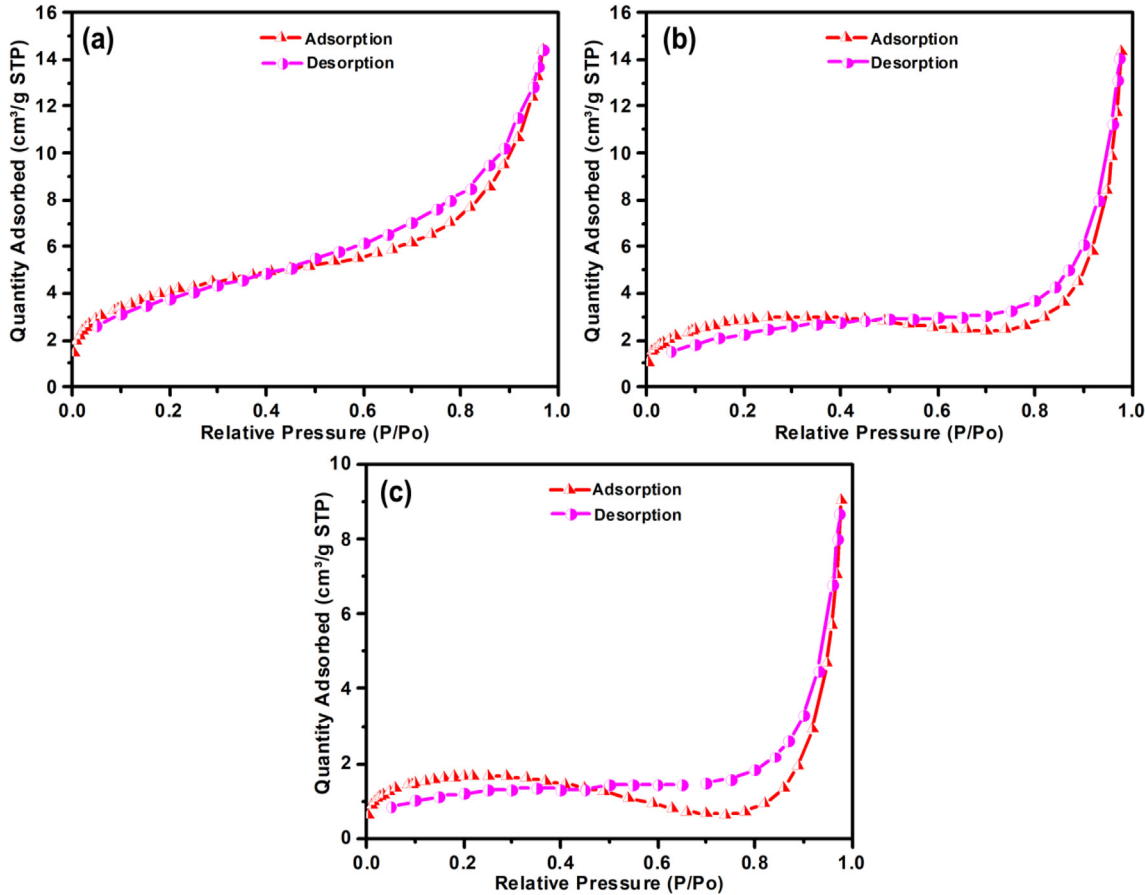


Fig. 5 – Nitrogen adsorption-desorption isotherms of (a) MIL-53(Fe), (b) ZnS@MIL-53(Fe) and (c) CdZnS@MIL-53(Fe)

Table 1 – BET and BJH parameters.

No.	Parameter	MIL-53(Fe)	ZnS@MIL-53(Fe)	CdZnS@MIL-53(Fe)
1	Single-point surface area at P/P ₀ m ² /g	14.19	9.91	5.91
2	BET surface area m ² /g	14.64	10.21	6.13
3	t-Plot external surface area m ² /g	13.64	7.49	2.87
4	BJH adsorption cumulative surface area of pores m ² /g	7.64	3.16	1.69
5	BJH desorption cumulative surface area of pores m ² /g	11.46	5.94	3.44
6	BJH adsorption cumulative volume of pores cm ³ /mg	19.30	18.82	7.37
7	BJH desorption cumulative volume of pores cm ³ /mg	19.87	21.18	8.88
8	Adsorption average pore width (4V/A by BET) nm	11.02	23.84	28.53
9	Desorption average pore width (4V/A by BET) nm	8.34	14.26	15.94
10	BJH adsorption average pore diameter (4V/A) nm	5.27	5.18	4.81
	BJH desorption average pore diameter (4V/A) nm	5.43	6.02	5.79

3.5. Electrochemical analysis of the oxygen evolution reaction (OER)

To investigate the oxygen evolution reaction (OER), cyclic voltammetry (CV) and linear sweep voltammetry (LSV) were performed at 10 and 1 mVs⁻¹, respectively. Fig. 6 (a-b) shows cyclic voltammetric curves of MIL-53(Fe), ZnS@MIL-53(Fe) and CdZnS@MIL-53(Fe) and their derivatives after thermal degradation. Of these three MOFs, CdZnS@MIL-53(Fe)/NF generates a maximum current density (577 mAcm⁻²) at 2 V applied potential (vs RHE) as compared to bare-MOF MIL-53(Fe)/NF (205 applied potential vs. RHE). The better OER activity of

CdZnS@MIL-53(Fe)/NF compared to the other synthesized materials is due to the formation of a heterojunction between the incorporated CdZnS and MIL-53(Fe), which reduces the electron-hole pair recombination, increases charge separation and enhances OER catalytic activity. Fig. 6 (b) shows the CV curves of the derivatives of the MOFs after heat treatment. The derivative of CdZnS@MIL-53(Fe), which was converted to CdZnS/Fe₂O₃, shows maximum activity after heat treatment due to the formation of a CdZnS/Fe₂O₃ heterojunction. The latter generates a maximum current density of 612 mAcm⁻² at 2 V applied potential (vs RHE) compared to the other decomposed products. Fig. 6 (c-d) represents the LSV curves of all the

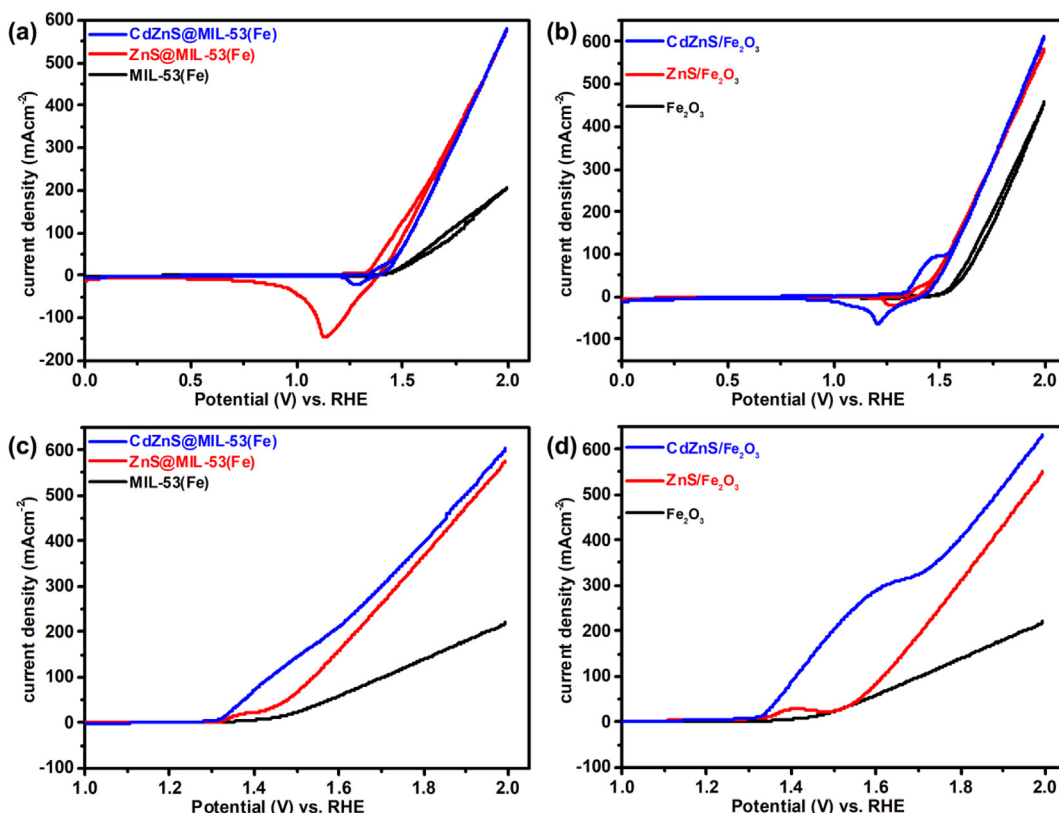
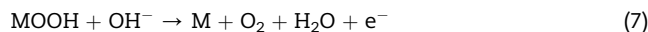


Fig. 6 – CV and LSV curves of (a,c) original MOFs MIL-53(Fe), ZnS@MIL-53(Fe) and CdZnS@MIL-53(Fe) and (b, d) MOF derivatives Fe₂O₃, ZnS/Fe₂O₃ and CdZnS/Fe₂O₃.

synthesized materials. CdZnS@MIL-53(Fe)/NF shows the lowest onset potential and generates maximum current density compared to the other MOFs. It requires a very low overpotential (95 mV) to deliver 10 mAcm⁻² current density compared to MIL-53(Fe)/NF (210 mV) and ZnS@MIL-53(Fe)/NF (112 mV). Similarly, the derivative of CdZnS@MIL-53(Fe), which converted to CdZnS/Fe₂O₃, shows the same behavior as the other decomposed derivatives. It requires very low overpotential (90 mV) to deliver 10 mAcm⁻² current density as compared to Fe₂O₃ (204 mV) and ZnS/Fe₂O₃ (115 mV).

Fig. 7 illustrates the basic mechanism of water splitting. In basic medium the oxygen evolution reaction, which is a half reaction of water splitting, takes place at the anode (working electrode). A four-step mechanism is proposed for oxygen evolution at the surface of the working electrode. During oxygen evolution three crucial intermediates (MOH, MO and MOOH) form as shown in Fig. 7(a) [45].



The figure indicates that evolution of oxygen gas and the formation of water take place at the surface of the anode.

As shown in Fig. 7(b) H⁺ is transferred to the counter electrode by an electrolyte and then undergoes reduction, resulting in the evolution of hydrogen gas. Considerable bubbling of the oxygen and hydrogen gas is also observed at the surface of the working electrode and the counter electrode, respectively. Based on the data in Table 2, it is possible to compare the OER activity of the synthesized samples with other materials.

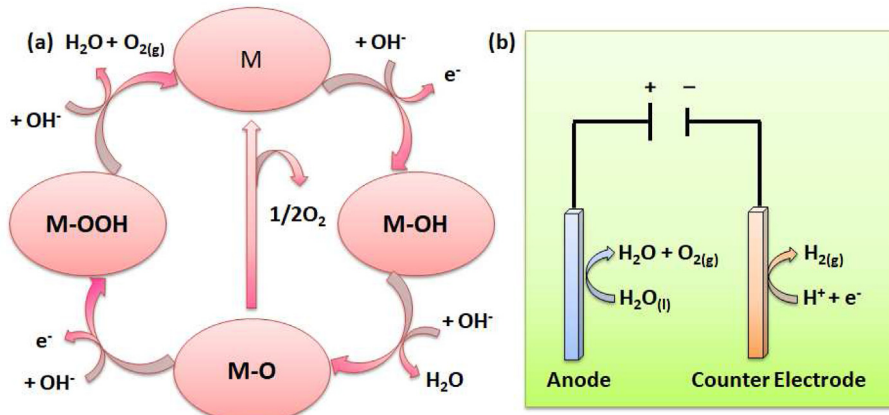


Fig. 7 – (a) OER mechanism of the electrocatalytic oxygen evolution reaction in basic medium and (b) schematic diagram of the electrochemical cell for the oxygen evolution reaction.

Table 2 – Comparison of OER of Fe-based catalysts in 1 M KOH.

Catalyst	Electrolyte	Overpotential (η_{10}) (mV)	Reference
NiS@MOF-5	1.0 M KOH	170	[24]
CoO _x /UiO-66-300	1.0 M KOH	283	[46]
NiO/UiO-66-300	1.0 M KOH	291.6	[46]
21 wt% W CoMoO ₄	1.0 M KOH	680	[47]
CoWO ₄ /GC	1.0 M KOH	388	[48]
CoWO ₄ /Ni	1.0 M KOH	336	[48]
Co _{0.5} Mn _{0.5} WO ₄	1.0 M KOH	400	[49]
FeCoNiO _x /NF	1.0 M KOH	203	[50]
CS-NiFe _{0.10} Cr _{0.10} on Cu	1.0 M KOH	200	[51]
NiCo ₂ O ₄ /NiO	1.0 M NaOH	360	[52]
N–NiFeOOH	1.0 M KOH	320	[53]
Co@Co ₃ O ₄ from ZIF-67	0.1 M KOH	410	[54]
Co ₃ O ₄ /NPC derived from ZIF-67/COF	1.0 M KOH	330	[55]
NiFe-NS	1.0 M KOH	304	[56]
FeNi NPs in N-doped carbon nanotubes	1.0 M KOH	300	[57]
CoP@RGO	1.0 M KOH	280	[58]
CeO ₂ /C	1.0 M KOH	297	[59]
CoO/Ce ₂ O ₃ @NH ₂ -UiO-66	1.0 M KOH	212	[60]
RuO ₂ Nanoparticles	1.0 M KOH	275	[61]
IrO ₂	1.0 M KOH	330	[62]
CdZnS@MIL-53(Fe)	1.0 M KOH	95	This Work
CdZnS/Fe ₂ O ₃	1.0 M KOH	90	This Work

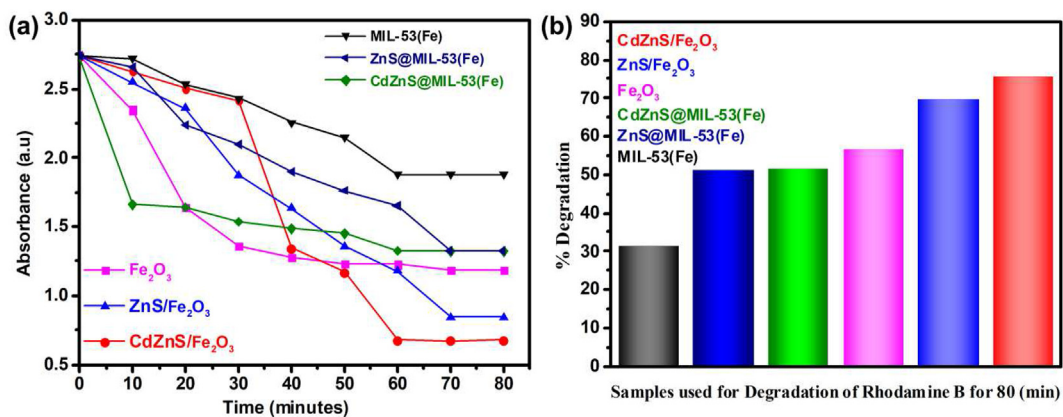


Fig. 8 – (a) Absorbance of light by Rhodamine B samples after adding MIL-53(Fe), ZnS@MIL-53(Fe), CdZnS@MIL-53(Fe), Fe₂O₃, ZnS/Fe₂O₃ and CdZnS/Fe₂O₃ for 80 min and (b) % photodegradation of Rhodamine B after 80 min.

3.6. Photocatalytic degradation of Rhodamine B

Photocatalytic degradation of Rhodamine B under 500W tungsten-lamp irradiation was studied to determine the photocatalytic activity of the prepared samples of MIL-53(Fe), ZnS@MIL-53(Fe), CdZnS@MIL-53(Fe) and their derivatives. The change in absorbance intensity at the characteristic wavelength (554 nm) of a Rhodamine B solution was measured by an UV-visible spectrophotometer. Fig. 8(a) shows the optical absorption of Rhodamine B dye solution using synthesized samples as photocatalysts. The measured absorbance decreased over time for all the samples, indicating the degradation of Rhodamine B. Similarly, the color of Rhodamine B changed over time for all the solutions. In the presence of MIL-53(Fe), the absorbance of light by the Rhodamine B dye solution decreased from 2.75 (a.u) to 1.85 (a.u) after 80 min. The absorbance of light by the ZnS@MIL-53(Fe), CdZnS@MIL-53(Fe), Fe₂O₃, ZnS/Fe₂O₃ and CdZnS/Fe₂O₃ samples was 1.32, 1.32, 0.84 and 0.67 (a.u), respectively. The maximum photocatalytic degradation efficiency of the CdZnS/Fe₂O₃ photocatalyst showed the least absorption of the Rhodamine B dye solution. Furthermore, the percentage of photodegradation of

all the synthesized materials was calculated according to the following formula

$$\% D = (A_o - A_t) / A_o \times 100 \quad (8)$$

where A_o = Initial Absorbance and A_t = Final Absorbance after 80 min. The calculated % photodegradation of Rhodamine B by MIL-53(Fe), ZnS@MIL-53(Fe), CdZnS@MIL-53(Fe) was 39, 45 and 51%, respectively. This shows that the incorporation of ZnS and CdZnS into Fe-based MOF increases the efficiency of photodegradation of Rhodamine B as a result of the formation of a heterojunction and the synergistic effect. The derivatives of these materials, obtained after thermal degradation, show better photocatalytic activity: 56, 69 and 75% photodegradation of Rhodamine B for the samples Fe₂O₃, ZnS/Fe₂O₃ and CdZnS/Fe₂O₃, respectively. Thus, CdZnS/Fe₂O₃ is the most efficient photocatalyst due to an acceptable band gap, the maximum use of visible light and a reduced recombination of electron-hole pairs. Based on the data in Table 3, it is possible to compare the photocatalytic activity of the synthesized samples with other materials.

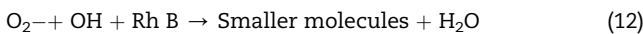
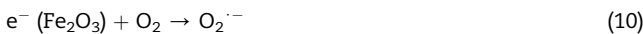
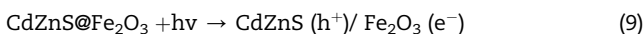
Table 3 – Comparison of % photodegradation of Rhodamine B by CdZnS@MIL-53(Fe) and its derivative, CdZnS/Fe₂O₃, with other photocatalytic materials.

Material	Time	Catalyst Dosage	PhB Concentration	%Degradation	References
Fe@Fe ₂ O ₃	12 h	0.2 g/L	15 mg/L	95	[63]
GR/MIL-53(Fe)	60 min	0.4 g/L	20 mg/L	41.6	[64]
Cu/Al ₂ O ₃ /g-C ₃ N ₄	120 min	1 g/L	20 mg/L	96	[65]
BiMnO ₃ /H ₂ O ₂ assisted	55 min	5 ppm	10 ppm	90	[66]
C, N-TiO ₂	90 min	3.6 g/L	20 mg/L	94	[67]
TiO ₂ on a β-SiC	120 min	Four foams	100 ppm	90	[68]
CdS/MIL-53(Fe)	120 min	0.5 g/L	10 mg/L	92.5	[69]
Co/Fe-MOF	120 min	0.05 g/L	14.3 mg/L	92	[70]
CdZnS@MIL-53(Fe)	80 min	0.2 g/L	47.9 mg/L	51	This work
CdZnS/Fe ₂ O ₃	80 min	0.2 g/L	47.9 mg/L	75	This work

3.7. Proposed mechanisms of photodegradation of Rhodamine B

CdZnS@MIL-53(Fe) and its thermally decomposed derivative were found to be the most efficient photocatalysts for the photodegradation of Rh B. Furthermore, the derivative of CdZnS@MIL-53(Fe) after heat treatment shows better photocatalytic activity due to the formation of the CdZnS/Fe₂O₃ heterojunction. In CdZnS/Fe₂O₃, the band gap of Fe₂O₃ is 2.1 eV and the values of the valence band (VB) and the conduction band (CB) are 2.43 and 0.33 eV, respectively [71]. On the other hand, the band gap of CdZnS is 3.0 eV and its VB and CB edges are present at 1.96 and -1.04 eV, respectively [72]. CB of CdZnS is more negative than CB of Fe₂O₃. Thus, under solar illumination, electrons are transferred from the VB of CdZnS to the CB and then to the conduction band of Fe₂O₃. Similarly, holes produced in the VB of Fe₂O₃ migrate toward the VB of CdZnS. Thus, the formation of a heterojunction increases charge separation and reduces the rate of recombination of electron-hole pairs. The electrons in the CB of Fe₂O₃ react with O₂ to form O₂⁻, because the potential of O₂/O₂⁻ is -0.33 eV vs NHE [73] and the holes in VB react with water and convert OH⁻ to OH (+2.40 eV vs NHE) [74].

These highly reactive species react with Rh B and convert it to smaller products and, finally, to H₂O and CO₂, while in the CdZnS@MIL-53(Fe) heterojunction, the band gap of MIL-53(Fe) is 2.83 eV and its VB and CB edges are at -0.36 and 2.47 eV, respectively. The CB of CdZnS is more negative than MIL-53(Fe). Thus, under solar illumination, the electrons jump from the VB of CdZnS to the CB and then to the CB of MIL-53(Fe). The VB and holes are transferred from the VB of MIL-53(Fe) to the VB of CdZnS. These heterojunctions improve the activity of CdZnS/Fe₂O₃ compared to CdZnS@MIL-53(Fe) because the CB potential (-0.31 eV) of Fe₂O₃ is closer to the standard redox potential ($E^\circ(O_2/O_2^-)$) = -0.33 eV and $E^\circ(O_2/HO^-)$ = -0.05 eV compared to the CB potential (-0.36 eV) of MIL-53(Fe). Thus, the electrons in the CB of Fe₂O₃ reduce the dissolved oxygen to superoxide anionic radicals of O₂⁻ much better than the CB of CdZnS@MIL-53(Fe); these radicals further oxidize the H₂O to hydroxyl radicals (OH). These highly active species oxidize the Rh B to CO₂ and H₂O. Further mechanism of photodegradation in detail, can be shown in below Equations;



3.8. Effect of incorporation of NPs on morphology and photocatalytic (electrochemical) activity of MIL-53(Fe)

As the SEM image shows, the bare MIL-53(Fe) grew with clearly defined and uniformly distributed polygonal crystals. It has a similar morphology after the in-situ incorporation of ZnS and CdZnS. The incorporation of ZnS and CdZnS into MIL-53(Fe) results in crystals with rougher surfaces. The incorporation

of ZnS and CdZnS into MOF MIL-53(Fe) leads to the development of the heterojunction and increases the electrocatalytic activity of MOF in the oxygen evolution reaction. This type of heterojunction was recently developed by Lu et al., who synthesized the efficient OER catalyst NiS@MOF-5, which delivereded 10 mAcm⁻² current density at a very low overpotential of 174 mV [24]. In another study the g-C₃N₄@MIL-125(Ti)/NF heterojunction delivered 10 mAcm⁻² current density at just 173 mV overpotential for the OER [75]. Our synthesized MIL-53(Fe)/NF requires 210 mV overpotential to deliver 10 mAcm⁻² current density. The UiO-66/MoS₂ hybrid delivers 10 mAcm⁻² current density at just 180 mV overpotential for the OER [76], while the ZnS@MIL-53(Fe)/NF and CdZnS@MIL-53(Fe)/NF require an ultralow overpotential of 112 and 95 mV to deliver 10 mAcm⁻² current density compared to MIL-53(Fe)/NF. The better OER activity of CdZnS@MIL-53(Fe)/NF compared to the other synthesized materials is due to the formation of the heterojunction between the incorporated CdZnS and the central metallic cluster of MIL-53(Fe), which reduces the electron-hole pair recombination, increases the charge separation and enhances the OER catalytic activity. Moreover, the synthesized samples MIL-53(Fe), ZnS@MIL-53(Fe) and CdZnS@MIL-53(Fe) showed potential activity for the photocatalytic degradation of Rhodamine B, which was investigated under solar irradiation (Fig. 8). The calculated percentage of the photodegradation of Rhodamine B by MIL-53(Fe), ZnS@MIL-53(Fe) and CdZnS@MIL-53(Fe) was 39, 45 and 51% respectively. This shows that the incorporation of ZnS and CdZnS into the Fe-based MOF increases the photodegradation of Rhodamine B as a result of the formation of a heterojunction and the synergistic effect. Hu et al. used the deposited CdS nanoparticles on MIL-53(Fe) for the photocatalytic degradation of Rhodamine B. Photodegradation of RhB was 92.4% after 120 min after addition of the catalyst: 0.5 g/L and Rhodamine B: 10 mg/L solution [69]. Tran et al. used the bimetallic Co/Fe-MOF for the photocatalytic degradation of Rhodamine B. Photodegradation of RhB was 92% 120 min after adding the catalyst: 0.05 g/L and Rhodamine B 14.3 mg/L solution [70]. In our experiment, the % photodegradation of RhB was determined after 80 min reaction time after adding the catalyst: 0.2 g/L and Rhodamine B: 47.9 mg/L solution. This indicates that our samples have better photocatalytic activity compared to the samples in other reported studies.

3.9. Effect of heat treatment on morphology and photocatalytic (electrochemical) activity of MIL-53(Fe)

The effect of heat treatment on morphology is clearly visible in the SEM images of MIL-53(Fe), ZnS@MIL-53(Fe) and CdZnS@MIL-53(Fe) (Fig. 4(d-f)). After heat treatment, all the materials had an irregular and distorted block-like shape with slight agglomeration. This indicates that the MOF structures were distorted, resulting in the formation of Fe₂O₃ and its heterojunctions with incorporated nanoparticles. The heterojunction between the incorporated nanoparticles and Fe₂O₃ derived from MOF increased the electrocatalytic activity of the oxygen evolution reaction. Nazar et al. derived cerium oxide/C from the metal organic framework, delivering 10 mAcm⁻² current density at low overpotential of 297 mV [59]. In another study the FeNi alloy nanoparticles encapsulated in N-doped

carbon nanotubes were obtained by thermal decomposition of ZIF-MOF. The current density reached 10 mA cm^{-2} at 300 mV overpotential for OER [57]. However, Charles et al. found that the OER activity of the $\text{CoO}_x/\text{UiO}-66$ and $\text{NiO}/\text{UiO}-66$ heterostructures decreased upon heat treatment due to the collapse of the MOF structure [46]. Our synthesized MIL-53(Fe)/NF required 210 mV overpotential to deliver 10 mA cm^{-2} current density, which decreased to 204 mV in the derivative Fe_2O_3 , while $\text{ZnS}/\text{Fe}_2\text{O}_3$ and $\text{CdZnS}/\text{Fe}_2\text{O}_3$ required an ultralow overpotential of 115 and 90 mV, respectively, to deliver 10 mA cm^{-2} current density compared to Fe_2O_3 . The better OER activity of $\text{CdZnS}/\text{Fe}_2\text{O}_3$ in comparison to the other materials is due to the formation of a heterojunction between the incorporated CdZnS and Fe_2O_3 , which reduces the recombination of the electron-hole pairs, increases the charge separation and enhances the OER catalytic activity. The incorporation of nanoparticles and heat treatment strongly enhanced the OER activity of Mil-53(Fe), thus making it far better than other OER electrocatalysts. Panda et al. developed $\text{Fe}_2\text{O}_3/\text{MIL-53(Fe)}$ and Fe_2O_3 by partial and complete decomposition of MIL-53(Fe); these catalysts were more effective for photocatalytic degradation [77]. Thus, the heat treatment of MIL-53(Fe), $\text{ZnS}@\text{MIL-53(Fe)}$ and $\text{CdZnS}@\text{MIL-53(Fe)}$ resulted in the derivatives Fe_2O_3 , $\text{ZnS}/\text{Fe}_2\text{O}_3$ and $\text{CdZnS}/\text{Fe}_2\text{O}_3$, respectively, with better activity for the photocatalytic degradation of Rhodamine B (Fig. 8). In heat-treated products, heterojunctions develop between the incorporated materials (ZnS and CdZnS) and Fe_2O_3 . This facilitates electron transfer at the interface and reduces the charge recombination, resulting in better photocatalytic activity. After 80 min reaction time after the addition of the catalyst (0.2 g/L and Rhodamine B: 47.9 mg/L solution), the calculated % photodegradation of Rhodamine B by Fe_2O_3 , $\text{ZnS}/\text{Fe}_2\text{O}_3$ and $\text{CdZnS}/\text{Fe}_2\text{O}_3$ was 56, 69, 75%, respectively. This indicates that the heterojunction between CdZnS and Fe_2O_3 and the synergistic effect increases the photodegradation efficiency of Rhodamine B.

4. Conclusion

In summary, $\text{CdZnS}@\text{MIL-53(Fe)}$ and its derivative $\text{CdZnS}/\text{Fe}_2\text{O}_3$ are highly active and stable electrocatalysts for oxygen evolution. The better OER activity of $\text{CdZnS}@\text{MIL-53(Fe)}/\text{NF}$ and $\text{CdZnS}/\text{Fe}_2\text{O}_3$ is attributed to the formation of a heterojunction between the incorporated CdZnS and the iron-containing metal-organic framework MIL-53(Fe) or Fe_2O_3 . This heterojunction reduces the recombination of the electron-hole pairs, increases the charge separation and enhances the OER catalytic activity by delivering the 10 mA cm^{-2} current density at ultralow overpotential. Moreover, the OER activity of $\text{CdZnS}@\text{MIL-53(Fe)}$ and its derivative $\text{CdZnS}/\text{Fe}_2\text{O}_3$ is at an acceptable level among the reported electrocatalysts. This work demonstrates the necessity for developing highly active catalysts for OER because they are more effective than current catalysts. $\text{CdZnS}/\text{Fe}_2\text{O}_3$ was effective in the photodegradation of Rhodamine B (up to 75% in just 80 min reaction time). We anticipate that a facile method of synthesizing highly efficient catalysts by in-situ incorporation and heat treatment will lead to new routes for water splitting and the photodegradation of organic dyes.

CRedit authorship contribution statement

Ghulam Asghar: Methodology, Writing, **Muhammad Fiaz:** Writing - review & editing, **Muhammad Asim Farid:** Writing - review & editing, **Muhammad Naeem Ashiq:** Formal analysis and **Muhammad Athar:** Conceptualization and Supervision.

Declaration of competing interest

The authors declare that they have no known competing financial interests or personal relationships that could have appeared to influence the work reported in this paper.

Acknowledgments

The authors acknowledge 1. Prof. Dr. Jeroen van Bokhoven of ETH-Zurich, Switzerland for providing the research facilities and 2. ScopeM, ETH-Zurich, Switzerland for electron microscopy.

REFERENCES

- [1] Abbasi T, Abbasi S. Decarbonization of fossil fuels as a strategy to control global warming. *Renew Sustain Energy Rev* 2011;15(4):1828–34.
- [2] Omri A, Nguyen DK. On the determinants of renewable energy consumption: international evidence. *Energy* 2014;72:554–60.
- [3] Veziroğlu TN, Şahin S. 21st Century's energy: hydrogen energy system. 2019.
- [4] Nicoletti G, Arcuri N, Nicoletti G, Bruno R. A technical and environmental comparison between hydrogen and some fossil fuels. *Energy Convers Manag* 2015;89:205–13.
- [5] Balat M. Potential importance of hydrogen as a future solution to environmental and transportation problems. *Int J Hydrogen Energy* 2008;33(15):4013–29.
- [6] Nejat Veziroglu T. Quarter century of hydrogen movement 1974–2000. *Int J Hydrogen Energy* 2000;25(12):1143–50.
- [7] Munawar T, Nadeem MS, Mukhtar F, Manzoor S, Ashiq MN, Batool S, et al. Enhanced photocatalytic, antibacterial, and electrochemical properties of CdO-based nanostructures by transition metals co-doping. *Adv Powder Technol* 2022;33(3):103451.
- [8] Schley ND, Blakemore JD, Subbaiyan NK, Incarvito CD, D'Souza F, Crabtree RH, et al. Distinguishing homogeneous from heterogeneous catalysis in electrode-driven water oxidation with molecular iridium complexes. *J Am Chem Soc* 2011;133(27):10473–81.
- [9] Park KS, Ni Z, Côté AP, Choi JY, Huang R, Uribe-Romo FJ, et al. Exceptional chemical and thermal stability of zeolitic imidazolate frameworks. *Proc Natl Acad Sci USA* 2006;103(27):10186–91.
- [10] Hu M, Ju Y, Liang K, Suma T, Cui J, Caruso F. Void engineering in metal–organic frameworks via synergistic etching and surface functionalization. *Adv Funct Mater* 2016;26(32):5827–34.
- [11] Rajaambal S, Sivarajanji K, Gopinath CS. Recent developments in solar H₂ generation from water splitting. *J Chem Sci* 2015;127(1):33–47.

- [12] Chi L, Xu Q, Liang X, Wang J, Su X. Iron-based metal–organic frameworks as catalysts for visible light-driven water oxidation. *Small* 2016;12(10):1351–8.
- [13] Liao C-H, Huang C-W, Wu J. Hydrogen production from semiconductor-based photocatalysis via water splitting. *Catalysts* 2012;2(4):490–516.
- [14] Xie YP, Yu ZB, Liu G, Ma XL, Cheng H-M. CdS–mesoporous ZnS core–shell particles for efficient and stable photocatalytic hydrogen evolution under visible light. *Energy Environ Sci* 2014;7(6):1895–901.
- [15] Nadeem MS, Munawar T, Mukhtar F, Batool S, Hasan M, Akbar UA, et al. Energy-levels well-matched direct Z-scheme ZnNiNdO/CdS heterojunction for elimination of diverse pollutants from wastewater and microbial disinfection. *Environ Sci Pollut Control Ser* 2022;29(33):50317–34.
- [16] Zhang J, Yu J, Zhang Y, Li Q, Gong JR. Visible light photocatalytic H₂-production activity of CuS/ZnS porous nanosheets based on photoinduced interfacial charge transfer. *Nano Lett* 2011;11(11):4774–9.
- [17] Abdi FF, Han L, Smets AHM, Zeman M, Dam B, van de Krol R. Efficient solar water splitting by enhanced charge separation in a bismuth vanadate–silicon tandem photoelectrode. *Nat Commun* 2013;4:2195–3001.
- [18] Yang G, Yan W, Zhang Q, Shen S, Ding S. One-dimensional CdS/ZnO core/shell nanofibers via single-spinneret electrospinning: tunable morphology and efficient photocatalytic hydrogen production. *Nanoscale* 2013;5(24):12432–9.
- [19] Huang X, Zafar A, Ahmad K, Hasan M, Tariq T, Gong S, et al. Biological synthesis of bimetallic hybrid nanocomposite: a remarkable photocatalyst, adsorption/desorption and antimicrobial agent. *Applied Surface Science Advances* 2023;17:100446.
- [20] Xu X, Hu L, Gao N, Liu S, Wageh S, Al-Ghamdi AA, et al. Semiconductors: controlled growth from ZnS nanoparticles to ZnS–CdS nanoparticle hybrids with enhanced photoactivity. *Adv Funct Mater* 2015;25(3):495–495.
- [21] Thibert A, Frame FA, Busby E, Holmes MA, Osterloh FE, Larsen DS. Sequestering high-energy electrons to facilitate photocatalytic hydrogen generation in CdSe/CdS nanocrystals. *J Phys Chem Lett* 2011;2(21):2688–94.
- [22] Huang L, Wang X, Yang J, Liu G, Han J, Li C. Dual cocatalysts loaded type I CdS/ZnS core/shell nanocrystals as effective and stable photocatalysts for H₂ evolution. *J Phys Chem C* 2013;117(22):11584–91.
- [23] Zhang H, Nai J, Yu L, Lou XWD. Metal–organic-framework-based materials as platforms for renewable energy and environmental applications. *Joule* 2017;1(1):77–107.
- [24] Fiaz M, Kashif M, Fatima M, Batool SR, Asghar MA, Shakeel M, et al. Synthesis of efficient TMS@MOF-5 catalysts for oxygen evolution reaction. *Catal Lett* 2020;150(9):2648–59.
- [25] Liu L, Zhang J, Cheng X, Xu M, Kang X, Wan Q, et al. Amorphous NH₂-MIL-68 as an efficient electro- and photo-catalyst for CO₂ conversion reactions. *Nano Res* 2023;16(1):181–8.
- [26] Ma TY, Dai S, Jaroniec M, Qiao SZ. Metal–organic framework derived hybrid Co₃O₄–carbon porous nanowire arrays as reversible oxygen evolution electrodes. *J Am Chem Soc* 2014;136(39):13925–31.
- [27] Yang J, Zhang F, Lu H, Hong X, Jiang H, Wu Y, et al. Hollow Zn/Co ZIF particles derived from core–shell ZIF-67@ZIF-8 as selective catalyst for the semi-hydrogenation of acetylene. *Angew Chem* 2015;127(37):11039–43.
- [28] Xue Y, Zheng S, Xue H, Pang H. Metal–organic framework composites and their electrochemical applications. *J Mater Chem A* 2019;7(13):7301–27.
- [29] Othman NW, Radde H, Puah PY, Ling YS, Moh PY. Enhancing photocatalytic activity of titanium dioxide through incorporation of MIL-53(Fe) toward degradation of organic dye. *J Chin Chem Soc* 2019;66(1):81–8.
- [30] Whitfield TR, Wang X, Liu L, Jacobson AJ. Metal–organic frameworks based on iron oxide octahedral chains connected by benzenedicarboxylate dianions. *Solid State Sci* 2005;7(9):1096–103.
- [31] Choi SH, An K, Kim EG, Yu JH, Kim JH, Hyeon T. Simple and generalized synthesis of semiconducting metal sulfide nanocrystals. *Adv Funct Mater* 2009;19(10):1645–9.
- [32] Horoz S, Akyol M, Ekicibil A, Sahin Ö. Structural, optical and magnetic properties of CdZnS and Ni:CdZnS nanoparticles. *J Mater Sci Mater Electron* 2017;28(23):18193–9.
- [33] Samal R, Kandasamy M, Chakraborty B, Rout CS. Experimental and theoretical realization of an advanced bifunctional 2D δ-MnO₂ electrode for supercapacitor and oxygen evolution reaction via defect engineering. *Int J Hydrogen Energy* 2021;46(55):28028–42.
- [34] Barrett EP, Joyner LG, Halenda PP. The determination of pore volume and area distributions in porous substances. I. Computations from nitrogen isotherms. *J Am Chem Soc* 1951;73(1):373–80.
- [35] Millange F, Guillou N, Walton RI, Grenèche J-M, Margiolaki I, Férey G. Effect of the nature of the metal on the breathing steps in MOFs with dynamic frameworks. *Chem Commun* 2008;39:4732–4.
- [36] Walton RI, Munn AS, Guillou N, Millange F. Uptake of liquid alcohols by the flexible FeIII metal–organic framework MIL-53 observed by time-resolved *in situ* X-ray diffraction. *Chem Eur J* 2011;17(25):7069–79.
- [37] Finger LW, Hazen RM. Crystal structure and isothermal compression of Fe₂O₃, Cr₂O₃, and V₂O₃ to 50 kbars. *J Appl Phys* 1980;51(10):5362–7.
- [38] Osuntokun J, Ajibade PA. Structural and thermal studies of ZnS and CdS nanoparticles in polymer matrices. *J Nanomater* 2016;2016.
- [39] Nivetha R, Kollu P, Chandar K, Pitchaimuthu S, Jeong SK, Grace AN. Role of MIL-53(Fe)/hydrated–dehydrated MOF catalyst for electrochemical hydrogen evolution reaction (HER) in alkaline medium and photocatalysis. *RSC Adv* 2019;9(6):3215–23.
- [40] Zhang C, Ai L, Jiang J. Solvothermal synthesis of MIL-53 (Fe) hybrid magnetic composites for photoelectrochemical water oxidation and organic pollutant photodegradation under visible light. *J Mater Chem A* 2015;3(6):3074–81.
- [41] Sharma R, Lamba S, Annapoorni S. Magnetic properties of polypyrrole-coated iron oxide nanoparticles. *J Phys Appl Phys* 2005;38(18):3354.
- [42] Suresh R, Giribabu K, Manigandan R, Stephen A, Narayanan V. Fabrication of Ni–Fe₂O₃ magnetic nanorods and application to the detection of uric acid. *RSC Adv* 2014;4(33):17146–55.
- [43] Sano H, Shono T, Sonoda H, Takatsu T, Ciucchi B, Carvalho R, et al. Relationship between surface area for adhesion and tensile bond strength – evaluation of a micro-tensile bond test. *Dent Mater* 1994;10(4):236–40.
- [44] Haul RS, Gregg J, Sing KSW. Adsorption, surface area and porosity. 2. Auflage, academic press, London 1982. 303 Seiten, Preis: \$ 49.50. Ber Bunsen Ges Phys Chem 1982;86(10):957–957.
- [45] Suen N-T, Hung S-F, Quan Q, Zhang N, Xu Y-J, Chen HM. Electrocatalysis for the oxygen evolution reaction: recent development and future perspectives. *Chem Soc Rev* 2017;46(2):337–65.

- [46] Charles V, Yang Y, Yuan M, Zhang J, Li Y, Zhang J, et al. CoO_x/UiO-66 and NiO/UiO-66 heterostructures with UiO-66 frameworks for enhanced oxygen evolution reactions. *New J Chem* 2021;45(32):14822–30.
- [47] Tantravivat D, Anuchai S, Ounnunkad K, Saipanya S, Aroonyadet N, Rujijanagul G, et al. Structural properties of tungsten-doped cobalt molybdate and its application in electrochemical oxygen evolution reaction. *J Mater Sci Mater Electron* 2018;29(15):13103–11.
- [48] Srirapu VKVP, Kumar A, Srivastava P, Singh RN, Sinha ASK. Nanosized CoWO₄ and NiWO₄ as efficient oxygen-evolving electrocatalysts. *Electrochim Acta* 2016;209:75–84.
- [49] Karkera G, Sarkar T, Bharadwaj MD, Prakash AS. Design and development of efficient bifunctional catalysts by tuning the electronic properties of cobalt–manganese tungstate for oxygen reduction and evolution reactions. *ChemCatChem* 2017;9(19):3681–90.
- [50] Bai L, Wen X, Guan J. Amorphous FeCoNi oxide for oxygen evolution reaction. *Mater Today Energy* 2019;12:311–7.
- [51] Fan L, Zhang P, Zhang B, Daniel Q, Timmer BJJ, Zhang F, et al. 3D core–shell NiFeCr catalyst on a Cu nanoarray for water oxidation: synergy between structural and electronic modulation. *ACS Energy Lett* 2018;3(12):2865–74.
- [52] Mahala C, Basu M. Nanosheets of NiCo₂O₄/NiO as efficient and stable electrocatalyst for oxygen evolution reaction. *ACS Omega* 2017;2(11):7559–67.
- [53] Li J, Song J, Huang B-Y, Liang G, Liang W, Huang G, et al. Enhancing the oxygen evolution reaction performance of NiFeOOH electrocatalyst for Zn-air battery by N-doping. *J Catal* 2020;389:375–81.
- [54] Ajiaz A, Masa J, Rösler C, Xia W, Weide P, Botz AJR, et al. Co@Co₃O₄ encapsulated in carbon nanotube-grafted nitrogen-doped carbon polyhedra as an advanced bifunctional oxygen electrode. *Angew Chem Int Ed* 2016;55(12):4087–91.
- [55] Zhuang G-L, Gao Y-f, Zhou X, Tao X-y, Luo J-m, Gao Y-j, et al. ZIF-67/COF-derived highly dispersed Co₃O₄/N-doped porous carbon with excellent performance for oxygen evolution reaction and Li-ion batteries. *Chem Eng J* 2017;330:1255–64.
- [56] Meng H, Ren Z, Du S, Wu J, Yang X, Xue Y, et al. Engineering a stereo-film of FeNi₃ nanosheet-covered FeOOH arrays for efficient oxygen evolution. *Nanoscale* 2018;10(23):10971–8.
- [57] Tao Z, Wang T, Wang X, Zheng J, Li X. MOF-derived noble metal free catalysts for electrochemical water splitting. *ACS Appl Mater Interfaces* 2016;8(51):35390–7.
- [58] Lv J, Yang X, Zang H-Y, Wang Y-H, Li Y-G. Ultralong needle-like N-doped Co(OH)F on carbon fiber paper with abundant oxygen vacancies as an efficient oxygen evolution reaction catalyst. *Mater Chem Front* 2018;2(11):2045–53.
- [59] Nazar N, Manzoor S, Yu Rehman, Bibi I, Tyagi D, Chughtai AH, et al. Metal-organic framework derived CeO₂/C nanorod arrays directly grown on nickel foam as a highly efficient electrocatalyst for OER. *Fuel* 2022;307:121823.
- [60] Kashif M, Fiaz M, Sajid MS, Gul F, Farid MA, Ashiq MN, et al. Functionalization of UiO-66-NH₂ by in-situ incorporation of nanomaterials to enhance photocatalytic efficiency towards oxygen evolution reaction. *Catal Lett* 2022;152(10):3202–12.
- [61] Dong G, Fang M, Zhang J, Wei R, Shu L, Liang X, et al. In situ formation of highly active Ni–Fe based oxygen-evolving electrocatalysts via simple reactive dip-coating. *J Mater Chem A* 2017;5(22):11009–15.
- [62] Huang J, Chen J, Yao T, He J, Jiang S, Sun Z, et al. CoOOH nanosheets with high mass activity for water oxidation. *Angew Chem Int Ed* 2015;54(30):8722–7.
- [63] Zhuang L, Zhou S, Yuan Y, Liu M, Wang Y. A novel bioelectro-Fenton system for coupling anodic COD removal with cathodic dye degradation. *Chem Eng J* 2010;163(1–2):160–3.
- [64] Zhang C, Ai L, Jiang J. Graphene hybridized photoactive iron terephthalate with enhanced photocatalytic activity for the degradation of rhodamine B under visible light. *Ind Eng Chem Res* 2015;54(1):153–63.
- [65] Zhou C, Liu Z, Fang L, Guo Y, Feng Y, Yang M. Kinetic and mechanistic study of rhodamine B degradation by H₂O₂ and Cu/Al₂O₃/g-C₃N₄ composite. *Catalysts* 2020;10(3):317.
- [66] Revathi B, Balakrishnan L, Pichaimuthu S, Nirmala Grace A, Krishna Chandar N. Photocatalytic degradation of rhodamine B using BiMnO₃ nanoparticles under UV and visible light irradiation. *J Mater Sci Mater Electron* 2020;31(24):22487–97.
- [67] Le TTT, Tran TD. Photocatalytic degradation of rhodamine B by C and N codoped TiO₂ nanoparticles under visible-light irradiation. *J Chem* 2020;2020:4310513.
- [68] Allé PH, Fanou GD, Robert D, Adouby K, Drogui P. Photocatalytic degradation of Rhodamine B dye with TiO₂ immobilized on SiC foam using full factorial design. *Appl Water Sci* 2020;10(9):207.
- [69] Hu L, Deng G, Lu W, Pang S, Hu X. Deposition of CdS nanoparticles on MIL-53(Fe) metal-organic framework with enhanced photocatalytic degradation of RhB under visible light irradiation. *Appl Surf Sci* 2017;410:401–13.
- [70] Ngan Tran TK, Ho HL, Nguyen HV, Tran BT, Nguyen TT, Thi Bui PQ, et al. Photocatalytic degradation of Rhodamine B in aqueous phase by bimetallic metal-organic framework M/Fe-MOF (M = Co, Cu, and Mg). *Open Chem* 2022;20(1):52–60.
- [71] Lingampalli S, Gautam UK, Rao C. Highly efficient photocatalytic hydrogen generation by solution-processed ZnO/Pt/CdS, ZnO/Pt/Cd_{1-x}Zn_xS and ZnO/Pt/CdS_{1-x}Se_x hybrid nanostructures. *Energy Environ Sci* 2013;6(12):3589–94.
- [72] Arif M, Li Q, Yao J, Huang T, Hua Y, Liu T, et al. Enhance photocatalysis performance and mechanism of CdS and Ag synergistic co-catalyst supported on mesoporous g-C₃N₄ nanosheets under visible-light irradiation. *J Environ Chem Eng* 2017;5(6):5358–68.
- [73] Huo P, Zhou M, Tang Y, Liu X, Ma C, Yu L, et al. Incorporation of N-ZnO/CdS/Graphene oxide composite photocatalyst for enhanced photocatalytic activity under visible light. *J Alloys Compd* 2016;670:198–209.
- [74] Oladipo AA. MIL-53 (Fe)-based photo-sensitive composite for degradation of organochlorinated herbicide and enhanced reduction of Cr (VI). *Process Saf Environ Protect* 2018;116:413–23.
- [75] Fiaz M, Carl N, Kashif M, Farid MA, Riaz NN, Athar M. Development of efficient bi-functional g-C₃N₄@MOF heterojunctions for water splitting. *RSC Adv* 2022;12(49):32110–8.
- [76] Ali M, Pervaiz E. Effect of synthesis route on electrocatalytic water-splitting activity of MoS₂/UiO-66 hybrid. *Mol Catal* 2022;519:112136.
- [77] Panda R, Rahut S, Basu JK. Preparation of a Fe₂O₃/MIL-53(Fe) composite by partial thermal decomposition of MIL-53(Fe) nanorods and their photocatalytic activity. *RSC Adv* 2016;6(84):80981–5.